

The impact of non-Gaussianity on the error covariance for observations of the Epoch of Reionization (EoR) 21-cm power spectrum

Abinash Kumar Shaw^{1,2★}, Somnath Bharadwaj^{1,2} and Rajesh Mondal³

¹Department of Physics, Indian Institute of Technology Kharagpur, Kharagpur 721302, India

²Centre For Theoretical Studies, Indian Institute of Technology Kharagpur, Kharagpur 721302, India

³Astronomy Centre, Department of Physics and Astronomy, University of Sussex, Brighton BN1 9QH, UK

Accepted XXX. Received YYY; in original form ZZZ

ABSTRACT

Recent simulations show the EoR 21-cm signal to be inherently non-Gaussian whereby the error covariance matrix \mathbf{C}_{ij} of the 21-cm power spectrum (PS) contains a trispectrum contribution which would be absent if the signal were Gaussian. Using the binned power spectrum and trispectrum from simulations, here we present a methodology for incorporating these with the baseline distribution and system noise to make error predictions for observations with any radio-interferometric array. Here we consider the upcoming SKA-Low. Non-Gaussianity enhances the errors introducing a positive deviation Δ relative to the Gaussian predictions. Δ increases with observation time t_{obs} and saturates as the errors approach the cosmic variance. Considering $t_{\text{obs}} = 1,024$ hrs where a 5σ detection is possible at all redshifts $7 \leq z \leq 13$, in the absence of foregrounds we find that the deviations are important at small k where we have $\Delta \sim 40 - 100\%$ at $k \sim 0.04 \text{ Mpc}^{-1}$ for some of the redshifts and also at intermediate k ($\sim 0.4 \text{ Mpc}^{-1}$) where we have $\Delta \sim 200\%$ at $z = 7$. Non-Gaussianity also introduces correlations between the errors in different k bins, and we find both correlations and anti-correlations with the correlation coefficient value spanning $-0.4 \leq r_{ij} \leq 0.8$. Incorporating the foreground wedge, Δ continues to be important ($> 50\%$) at $z = 7$. We conclude that non-Gaussianity makes a significant contribution to the errors and this is important in the context of the future instruments which aim to achieve high sensitivity measurements of the EoR 21-cm PS.

Key words: cosmology: reionization—first stars—large-scale structure of universe—diffuse radiation, methods: statistical, technique: interferometric

1 INTRODUCTION

The Epoch of Reionization (EoR) is an important but poorly understood milestone in the cosmic history when the Hydrogen in the universe underwent a transition from neutral (H I) to ionized (H II) phase. Our current knowledge of the EoR comes from several indirect observations. The measurements of the Thomson scattering optical depth $\tau_{\text{Th}} = 0.058 \pm 0.012$ (Planck Collaboration et al. 2016a,b) of the cosmic microwave background radiation (CMBR) with the free electrons in the intergalactic medium (IGM) suggests that the universe was ionized at less than 10% level at redshifts above $z \sim 10$. Measurements of the high redshift quasar spectra (Becker et al. 2001; Fan et al. 2002, 2006; Gallerani et al. 2006; Becker et al. 2015) show a complete Gunn-Peterson trough and also measurements of the Gunn-Peterson optical depth τ_{GP} suggest that the reionization was over by $z \sim 6$. Recent studies of the Ly- α emitters (LAE) show a rapid decline in the luminosity function

at $z \geq 6$ (Ouchi et al. 2010; Jensen et al. 2014; Konno et al. 2014; Faisst et al. 2014; Santos et al. 2016; Ota et al. 2017; Zheng et al. 2017) which suggests a rapid increase in the H I density in the IGM and a patchy H I distribution at those redshifts. These indirect observations together suggest the reionization to occur within a redshift range $6 \leq z \leq 12$ (Mitra et al. 2013; Robertson et al. 2013; Mitra et al. 2015; Robertson et al. 2015; Mondal et al. 2016; Dai et al. 2018). However such indirect observations are not adequate to address many fundamental issues related to the EoR such as the exact duration and timing, the properties of the ionizing sources and the topology of H I distribution.

Observations of the redshifted 21-cm radiation due to the hyperfine transition of H I is a promising probe to study the high redshift universe (Sunyaev & Zeldovich 1972; Scott & Rees 1990). The low frequency radio interferometers will measure brightness temperature fluctuations of the EoR 21-cm radiation (Bharadwaj & Sethi 2001; Bharadwaj & Ali 2005). A substantial effort is currently underway to measure the EoR 21-cm signal using

★ E-mail: abinashkumarshaw@iitkgp.ac.in

the first generation radio interferometers e.g. GMRT¹ (Paciga et al. 2013), MWA² (Jacobs et al. 2016), LOFAR³ (Yatawatta, S. et al. 2013), PAPER⁴ (Ali et al. 2015) and the second generation interferometers such as HERA⁵ (Pofer et al. 2014; Ewall-Wice et al. 2016) and the upcoming gigantic SKA⁶ (Koopmans et al. 2014). These experiments aim to measure the EoR 21-cm power spectrum (PS) (Bharadwaj & Ali 2004). The expected EoR 21-cm signal is about 4–5 orders of magnitude weaker compared to the galactic and extra-galactic foregrounds (Ali et al. 2008; Bernardi, G. et al. 2009, 2010; Ghosh et al. 2012; Paciga et al. 2013; Beardsley et al. 2016). The foregrounds together with the system noise and other calibration errors pose a huge challenge for the measurement of the EoR 21-cm PS. Only weak upper limits on the EoR 21-cm PS have been estimated till date (McGreer et al. 2011; Parsons et al. 2014; Pofer et al. 2016a). In addition to the PS, various other statistics such as the variance (Patil et al. 2014), bispectrum (Yoshiura et al. 2015; Shimabukuro et al. 2017; Majumdar et al. 2018) and the Minkowski Functional (Kapahtia et al. 2018; Bag et al. 2018) has been proposed to quantify the EoR 21-cm signal.

In the recent past several works have made quantitative predictions of the sensitivity for measuring the EoR 21-cm PS (Morales & Hewitt 2004). McQuinn et al. (2006) have made predictions for 1,000 hrs of observations with the MWA, LOFAR and the upcoming SKA-Low. Beardsley et al. (2013) have estimated that MWA is capable of detecting the EoR 21-cm signal at $\sim 14\sigma$ level with ~ 900 hrs of observations. Zaroubi et al. (2012) have made quantitative predictions for sensitivity of LOFAR considering 600 hrs of observations, and Jensen et al. (2013) have predicted that LOFAR will be able to detect the EoR 21-cm PS at $k \sim 0.1 \text{ Mpc}^{-1}$ with $\sim 1,000$ hrs of observations. Parsons et al. (2012) have predicted that the EoR 21-cm signal can be detected at $k \sim 0.2 h \text{ Mpc}^{-1}$ with PAPER in 7 months of observations. The results of Pofer et al. (2014) suggest that the upcoming HERA will be able to detect the EoR 21-cm PS at a level $\sim 30\sigma$ within the k range $0.1 - 1 \text{ Mpc}^{-1}$ assuming a moderate foreground model. Ewall-Wice et al. (2016) have studied the prospects of detecting the EoR 21-cm PS with HERA incorporating X-ray heating of the IGM.

The upcoming SKA-Low, to be located in Australia, will be the most sensitive radio telescope to be built. It will have 513 stations, each of which combines the signal from several constituent log periodic dipole antennas. Each of these station is planned to be ~ 35 m in diameter. The telescope will operate within a frequency band of 50–350 MHz and it will have $\sim 20 \text{ deg}^2$ field of view. The interferometer will have a compact core and 3 spiral arms which will extend up to a large distance such that maximum antenna separation is ~ 60 km. A recent study by Mellema et al. (2013) has quantified the prospects of detecting the EoR 21-cm PS with SKA-Low. The authors have predicted the errors in the measured EoR 21-cm PS at three different redshifts 8, 10, and 12. In this analysis they have varied the number of core antennas and also the core radius. The analysis incorporates the system noise assuming 1,000 hrs of observation with a bandwidth of 10 MHz. They find that it will be possible to achieve a maximum SNR of ~ 100 at $k \sim 0.4 \text{ Mpc}^{-1}$ for all the three redshifts. They also find that the

predictions for SKA-Low show a significant improvement in comparison with other precursor telescopes such as MWA, LOFAR and PAPER (Fig. 21 and 22 of Mellema et al. 2013).

All the existing predictions for detecting the EoR 21-cm PS have assumed the signal to be a Gaussian random field. This assumption plays a crucial role in making the predictions. The PS completely specifies the statistical properties of the signal for a Gaussian random field, and this assumption allows the signal in each Fourier mode to be treated as being independent. Gaussianity is possibly a good assumption during the early stages of EoR, and also when one observe very large length-scales. However the growth and subsequent overlapping of the H II regions make the signal highly non-Gaussian as reionization progresses (Bharadwaj & Pandey 2005). The PS no longer quantifies the entire statistical properties of the signal as the signal in different Fourier modes are correlated. Higher order statistics like the bispectrum (Majumdar et al. 2018) and trispectrum are needed to quantify these correlations. This also affects the error predictions for the PS. Considering only cosmic variance (CV) which is inherent to the signal, Mondal et al. (2015) have studied the effects of non-Gaussianity on the error predictions for the EoR 21-cm PS. For a Gaussian random field, the SNR for the 21-cm PS is expected to increase as the square root of the number of independent Fourier modes. However, Mondal et al. (2015) find that as a consequence of the non-Gaussianity the SNR saturates at a limiting value $[\text{SNR}]_l$ beyond which it does not increase any further. The value of $[\text{SNR}]_l$ was also found to decreases with the progress of reionization which corresponds to an increase in the non-Gaussianity. Two subsequent papers (Mondal et al. 2016, 2017) have quantified the error covariance for the binned PS which now has an extra contribution from the trispectrum as compared to the Gaussian situation where the error covariance can be expressed entirely in terms of the PS. In these papers they have developed a unique statistical technique for estimating the bin-averaged trispectrum from the PS error covariance. They have used an ensemble of semi-numerical EoR simulations to estimate the error covariance and the trispectrum at several redshifts in the range $7 \leq z \leq 13$. The trispectrum contribution is found to increase significantly as reionization progresses. The non-Gaussianity is found to result in larger error estimates compared to the Gaussian predictions. Non-Gaussianity also introduces correlations between the PS error estimates at different bins.

In this paper, we predict the prospects of measuring the EoR 21-cm PS using observations with the upcoming SKA-Low. To this end we study the error covariance of the EoR 21-cm PS that will be measured by SKA-Low. Unlike the previous works (e.g. Mellema et al. 2013), our analysis incorporates the inherent non-Gaussian nature of the signal. We have used the EoR 21-cm PS and trispectrum from the simulations of Mondal et al. 2017. We include the system noise contribution to calculate the full PS error covariance for the current proposed configuration of SKA-Low⁷. The analysis in this paper also incorporates the impact of foregrounds considering the EoR 21-cm signal to be free of other possible calibration errors.

The structure of this paper is as follows. Section 2 briefly describes the simulations and the techniques used in Mondal et al. 2017 to obtain the EoR 21-cm PS and trispectrum. Section 3 briefly presents the SKA-Low configuration and discusses how to combine the observed visibility data for an optimal estimate of the EoR 21-cm PS. We also present a framework to compute the EoR 21-cm

¹ <http://www.gmrt.ncra.tifr.res.in>

² <http://www.haystack.mit.edu/ast/arrays/mwa>

³ <http://www.lofar.org>

⁴ <http://eor.berkeley.edu>

⁵ <http://reionization.org>

⁶ <http://www.skatelescope.org>

⁷ [SKA1_LowConfigurationCoordinates-1.pdf](#)

PS error covariance. Section 4 presents the results considering no foregrounds. In section 5 we study the effects of foregrounds and finally summarize and discuss our findings in Section 6. In keeping with the simulations of Mondal et al. 2017, we have used the Planck+WP (Planck Collaboration et al. 2014) best fit cosmological parameters throughout this paper.

2 SIMULATING THE EoR 21-cm SIGNAL

We have simulated the EoR 21-cm signal at six different redshifts $z = 13, 11, 10, 9, 8$ and 7 using a semi-numerical technique (Majumdar et al. 2013; Mondal et al. 2015) which comprises of three major steps. First, we generate the dark matter distributions at the aforementioned redshifts using a publicly available particle mesh N -body code⁸ (Bharadwaj & Srikant 2004). We have simulated the dark matter distributions within a cube of comoving volume $V = [215.04 \text{ Mpc}]^3$ with a grid size of 0.07 Mpc and a mass resolution of $1.09 \times 10^8 M_\odot$. Next, we identify the dark matter halos within the matter distribution using a publicly available halo finder⁹ based on the Friends-of-Friend (FoF) algorithm (Davis et al. 1985) with a linking length 0.2 times the mean inter-particle spacing and a minimum halo mass of $1.09 \times 10^9 M_\odot$ which corresponds to ten simulation particles. In the final step we generate the reionization map using a publicly available semi-numerical code¹⁰ following the formalism adopted by Choudhury et al. (2009). We assume that the hydrogen traces the dark matter, and the halos with masses exceeding a minimum halo mass M_{\min} ($M \geq M_{\min}$) host the ionizing sources, the number of ionizing photons N_γ emitted by a source being proportional to the host halo mass M through a dimensionless constant of proportionality N_{ion} which incorporates a large number of unknown parameters like the star formation efficiency and the UV photon escape fraction.

The hydrogen and photon densities are respectively smoothed over spheres of radius R . Any grid point within the simulation is considered to be completely ionized if the smoothed photon density exceeds the smoothed hydrogen density, the smoothing radius is allowed to vary from one grid spacing to a maximum value of R_{mfp} . The resulting H I distribution is mapped to redshift space using the prescription of Majumdar et al. 2013 to generate the final 21-cm brightness temperature distribution on a grid eight times coarser than the N -body simulation. The simulations used here are exactly the same as those which were used in Mondal et al. (2016, 2017) and the reader is referred to there for further details. These simulations have three free parameters namely M_{\min} the minimum halo mass, N_{ion} the ionizing efficiency and R_{mfp} the mean free path of the ionizing photons. We have used the values $M_{\min} = 1.09 \times 10^9 M_\odot$, $N_{\text{ion}} = 23.21$ and $R_{\text{mfp}} = 20 \text{ Mpc}$ (Songaila & Cowie 2010) to obtain a reionization history where the mean mass averaged neutral fraction has a value $\bar{x}_{\text{HI}} = 0.5$ at $z = 8$ and is over by $z \sim 6$. The integrated Thomson scattering optical depth obtained using these parameter values, $\tau = 0.057$ is also consistent with the observations (Planck Collaboration et al. 2016a) where $\tau = 0.058 \pm 0.012$.

3 POWER SPECTRUM ERROR COVARIANCE

We quantify the statistics of the EoR 21-cm brightness temperature fluctuations using the power spectrum (PS) which is defined as $P(k) = V^{-1} \langle \tilde{T}_b(\mathbf{k}) \tilde{T}_b(-\mathbf{k}) \rangle$. Here V is the simulation (observational) volume, $\tilde{T}_b(\mathbf{k})$ is the Fourier transform of the brightness temperature fluctuations $\delta T_b(\mathbf{x})$ and \mathbf{k} is a wave vector. In the absence of foregrounds and calibration errors, the brightness temperature fluctuations recorded by a radio interferometer is $\tilde{T}_t(\mathbf{k}) = \tilde{T}_b(\mathbf{k}) + \tilde{T}_N(\mathbf{k})$ which is a sum of the 21-cm signal $\tilde{T}_b(\mathbf{k})$ and the system noise contribution $\tilde{T}_N(\mathbf{k})$. The PS corresponding to $\tilde{T}_t(\mathbf{k})$ therefore is a sum of $P(k)$ and $P_N(k)$ which is the system noise PS *i.e.* $P_t(k) = [P(k) + P_N(k)]$. We have used the simulations described in section 2 to predict the EoR 21-cm PS $P(k)$. In the present work we make predictions for the upcoming SKA-Low⁷, and we have used the specification described in the subsequent paragraph to compute the noise PS $P_N(k)$. We have considered the upcoming SKA-Low to be an array of 513 stations⁷, each of which is a station of diameter $D = 35 \text{ m}$. The instrument will operate within a frequency range of 50–350 MHz which will probe the H I 21-cm signal between $z = 27$ and $z = 3$. The EoR 21-cm signal evolves significantly along the line-of-sight (LoS) and observations at different redshifts will probe the signal at different stages of reionization due to the light cone effect (Datta et al. 2012, 2014). As a consequence the signal no longer remains ergodic along the LoS and there is a significant loss of information if the entire frequency band is used to estimate the PS (Mondal et al. 2018; Mondal et al. 2019). In the present work we have avoided this by restricting the analysis to six different redshift slices each of width $\Delta z = 0.75$ centered at redshifts $z = 13, 11, 10, 9, 8$ and 7. We have also assumed that the entire frequency bandwidth is divided into frequency channels of width $\Delta \nu_c = 0.1 \text{ MHz}$. Note that the antenna layout, number of antennas and the channel width $\Delta \nu_c$ assumed here are only representative values, and may change in the final implementation of the telescope.

The analysis in this paper considers an observation tracking a field at declination $\text{DEC} = -30^\circ$ using SKA-Low for 8 hrs with 60 sec integration time. The 60 sec integration time has been chosen here to keep the simulated baseline data volume small. However the purpose of simulating the array baseline configuration here is to primarily estimate $P_N(k)$, and we find that the noise predictions do not show any noticeable change even when the integration time is reduced to 30 sec or to 15 sec. Considering \mathbf{d} to be the projection of the antenna separation on the plane perpendicular to the LoS, we use $\mathbf{U} = \mathbf{d}/\lambda_c$ with λ_c being the wavelength which corresponds to the central frequency ν_c of a slice. The subsequent analysis is restricted to the baselines \mathbf{U} corresponding to the antenna separations $|\mathbf{d}| \leq 19 \text{ km}$ as the baseline distribution falls off rapidly at larger values of \mathbf{d} . The simulated observations provide us the baselines \mathbf{U}_i and frequency channels ν_n at which the signal will be measured. We use $\mathbf{k}_{\perp i} = (2\pi \mathbf{U}_i)/r_c$ and $k_{\parallel m} = (2\pi m)/(r'_c B)$ with $0 \leq m \leq N_c/2$ where r_c is the comoving distance to the center of a redshift slice, $r'_c = \partial r / \partial \nu|_{\nu=\nu_c}$, B is the frequency bandwidth of the redshift slice and $N_c = B/\Delta \nu_c$. Note that $k_{\parallel m}$ is the Fourier conjugate of $r'_c(\nu_n - \nu_c)$. The simulations provide us with a set of comoving vectors $(\mathbf{k}_{\perp i}, k_{\parallel m})$ at which we will obtain measurements of the brightness temperature fluctuations $\tilde{T}_b(\mathbf{k}_{\perp i}, k_{\parallel m})$. Two different baselines having separation less than D/λ_c do not have independent information due to overlap of the antenna beam pattern (Bharadwaj & Ali 2005). We grid the comoving wave vectors with a grid of size $\Delta k_x = \Delta k_y = (2\pi D)/(\lambda_c r_c)$ and $\Delta k_z = (2\pi)/(r'_c B)$. Considering a grid point \mathbf{k}_g , we define $\tau(\mathbf{k}_g)$ to be the number of mea-

⁸ <https://github.com/rajeshmondal18/N-body>

⁹ <https://github.com/rajeshmondal18/FoF-Halo-finder>

¹⁰ <https://github.com/rajeshmondal18/ReionYuga>

measurements which lie within a voxel centered at \mathbf{k}_g . We use $\tau(\mathbf{k}_g)$ to estimate the noise PS $P_N(\mathbf{k}_g)$ at each grid point \mathbf{k}_g using the following expression (Chatterjee & Bharadwaj 2018)

$$P_N(\mathbf{k}_g) = \frac{r_c^2 r'_c T_{\text{sys}}^2 \lambda_c^2}{N_p N_t \Delta t \chi A_g \tau(\mathbf{k}_g)} = \frac{8 \text{ hrs}}{t_{\text{obs}}} \times \frac{P_0}{\tau(\mathbf{k}_g)}. \quad (1)$$

Here T_{sys} is the system temperature, N_p is the number of polarizations, N_t is the number of observed nights with 8 hrs per night, Δt is the integration time, $A_g = (\pi D^2)/4$ is the geometric area of a single antenna. It is convenient to quantify the total duration of the observations using $t_{\text{obs}} = N_t \times 8 \text{ hrs}$ instead of N_t , and we have used t_{obs} through the subsequent discussion of this paper. The system temperature $T_{\text{sys}} = T_{\text{sky}} + T_{\text{rec}}$ is a sum of the sky temperature $T_{\text{sky}} = 60 \lambda^{2.55} \text{ K}$ (Fixsen et al. 2011) and the receiver temperature $T_{\text{rec}} = 100 \text{ K}$. Here χ is defined using

$$\frac{1}{\chi} = \frac{A_g}{\lambda_c^2} \frac{[\int d\Omega A(\theta)]^2}{[\int d\Omega A^2(\theta)]} \quad (2)$$

where $A(\theta)$ is the telescope's primary beam pattern (Sarkar & Bharadwaj 2013; Parsons et al. 2014). We have approximated the beam pattern with a Gaussian $e^{-(\theta/\theta_0)^2}$ (Choudhuri et al. 2014) and evaluated the solid angle integral in the flat sky approximation to obtain $\chi = 0.53$. Note that $P_N(\mathbf{k}_g)$ is infinitely large at the grid points where $\tau(\mathbf{k}_g) = 0$ i.e. the grid points which are not sampled by the telescope baseline distribution.

Considering a typical SKA-Low observation spanning an angular extent of $\sim 3^\circ \times 3^\circ$ on the sky with an angular resolution $\sim 1'$ and a frequency bandwidth of $\sim 64 \text{ MHz}$ with frequency resolution $\sim 0.1 \text{ MHz}$, this corresponds to $N_k = [180 \times 180 \times 640] \approx 2 \times 10^7$ different grid points at which the EoR 21-cm PS will be measured. The dimension of the resulting PS error covariance matrix is $\sim 10^7 \times 10^7$ which renders further computations prohibitively expensive if not impossible. In order to overcome the intractability of such a large covariance matrix we bin the \mathbf{k} space and use the binned PS estimator which, for the i -th bin, is defined as

$$\hat{P}_t(k_i) = V^{-1} \sum_g w_g \tilde{T}_t(\mathbf{k}_g) \tilde{T}_t(-\mathbf{k}_g), \quad (3)$$

where the sum is over the \mathbf{k}_g modes within the i -th bin and w_g is the normalized weight associated with each mode with $\sum_g w_g = 1$. Here $k_i = \sum_g w_g k_g$ is the average k value corresponding to the i -th bin. The weights w_g have been introduced to account for the fact that the ratio $P(\mathbf{k}_g)/P_N(\mathbf{k}_g)$ varies across the different grid points, and as discussed later, the weights have been chosen so as to maximize the SNR of the bin-averaged PS. For the present analysis we have divided the available \mathbf{k} space into ten logarithmic spherical bins. The ensemble average of $\hat{P}_t(k_i)$ gives the bin-averaged PS $\bar{P}_t(k_i) = \langle \hat{P}_t(k_i) \rangle = \bar{P}(k_i) + \bar{P}_N(k_i)$. Note that the resulting estimate has a noise bias $\bar{P}_N(k_i)$, this however can be eliminated by suitably modifying the estimator (Choudhuri et al. 2016b). In the subsequent analysis we assume that the noise bias has been eliminated and we have an unbiased estimate of the bin-averaged power spectrum $\bar{P}(k_i)$. The noise contribution to the PS error covariance $\mathbf{C}_{ij} = \langle [\hat{P}_t(k_i) - \bar{P}_t(k_i)][\hat{P}_t(k_j) - \bar{P}_t(k_j)] \rangle$, however, cannot be eliminated and following the calculation presented in Mondal et al. (2016), we have

$$\begin{aligned} \mathbf{C}_{ij} = & \sum_{g_i} w_{g_i}^2 [P(\mathbf{k}_{g_i}) + P_N(\mathbf{k}_{g_i})]^2 \delta_{ij} \\ & + V^{-1} \sum_{g_i} \sum_{g_j} w_{g_i} w_{g_j} T(\mathbf{k}_{g_i}, -\mathbf{k}_{g_i}, \mathbf{k}_{g_j}, -\mathbf{k}_{g_j}), \end{aligned} \quad (4)$$

where the sum is over the grids points \mathbf{k}_{g_i} and \mathbf{k}_{g_j} in the i -th and the j -th bins respectively. The trispectrum $T(\mathbf{k}_1, -\mathbf{k}_2, \mathbf{k}_3, -\mathbf{k}_4)$ originates due to non-Gaussianity of the EoR 21-cm signal, the quantity which appears here is the weighted bin-averaged trispectrum. For the diagonal terms of the covariance matrix \mathbf{C}_{ij} the trispectrum quantifies the excess with respect to the Gaussian predictions. The off-diagonal terms of \mathbf{C}_{ij} are predicted to be zero if the EoR 21-cm signal were a Gaussian random field. The trispectrum arising due to the non-Gaussianity introduce non-zero off-diagonal terms corresponding to correlations (and anti-correlations) between the errors in the PS estimates in the different k bins (Mondal et al. 2016, 2017). The system noise has been considered to be outcome of a Gaussian random process and this does not contribute to the non-Gaussianity through the trispectrum.

3.1 Computing the Error Covariance from the Simulations

The PS error covariance \mathbf{C}_{ij} consists of two components – (1) the cosmic variance, and (2) the system noise. According to the equation (4) we need the EoR 21-cm PS $P(\mathbf{k}_g)$, the EoR 21-cm trispectrum $T(\mathbf{k}_{g_i}, -\mathbf{k}_{g_i}, \mathbf{k}_{g_j}, -\mathbf{k}_{g_j})$, the noise PS $P_N(\mathbf{k}_g)$ and appropriate weights w_g to compute the \mathbf{C}_{ij} . The reionization simulations of Mondal et al. (2017) provide us the bin-averaged EoR 21-cm PS

$$\bar{P}(k_i) = N_{k_i}^{-1} \sum_{g_i} P(\mathbf{k}_{g_i}) \quad (5)$$

and the bin-averaged trispectrum

$$\bar{T}(k_i, k_j) = (N_{k_i} N_{k_j})^{-1} \sum_{g_i} \sum_{g_j} T(\mathbf{k}_{g_i}, -\mathbf{k}_{g_i}, \mathbf{k}_{g_j}, -\mathbf{k}_{g_j}), \quad (6)$$

where the sum in equation (6) is over the grid points (\mathbf{k}_g modes) in the i -th and j -th bins, and the N_{k_i} and N_{k_j} are numbers of grid points in the respective bins. The bins that we have chosen to analyze the simulated SKA-Low observations have exactly the same boundaries as the bins used to analyze the EoR simulations in Mondal et al. (2017), however we cannot directly use the $\bar{P}(k_i)$ and $\bar{T}(k_i, k_j)$ from Mondal et al. (2017) in equations (3) and (4) to predict the PS error covariance for the SKA-Low observations. First, equations (5) and (6) assume uniform weights whereas it is necessary to consider the variation of w_g across the grid points to account for the non-uniform sampling when considering the simulated observations (equations 3 and 4). Further, the resolution of the simulations and the observations will, in general, be different and consequently the \mathbf{k} grid spacing will also differ.

One can attempt to estimate the ensemble averages of $P(\mathbf{k}_g)$ at every individual grid point and $T(\mathbf{k}_{g_i}, -\mathbf{k}_{g_i}, \mathbf{k}_{g_j}, -\mathbf{k}_{g_j})$ at every pair of grid points, however these estimates will be extremely noisy due to the limited number of statistically independent realizations in the EoR 21-cm signal ensemble (e.g. 50 in Mondal et al. 2017). Further, we have an enormous volume of the trispectrum data which renders this approach unfeasible. The issue now is to predict the bin-averaged PS (equation 3) and its error covariance (equation 4) for the SKA-Low observations using the results (equations 5 and 6) from the simulations of Mondal et al. (2017).

Here we have assumed that the EoR 21-cm PS does not vary much across the grid points \mathbf{k}_{g_i} within a bin (say the i -th bin), and in equations (3) and (4) we have used the simulated $\bar{P}(k_i)$ from Mondal et al. (2017) to calculate $P(\mathbf{k}_{g_i}) = \bar{P}(k_i)$ for all the grid points in the i -th bin. The value of $T(\mathbf{k}_{g_i}, -\mathbf{k}_{g_i}, \mathbf{k}_{g_j}, -\mathbf{k}_{g_j})$ in equation (4) depends on the magnitude and direction of the two vectors \mathbf{k}_{g_i}

and \mathbf{k}_g , and both of these can vary widely even when the two vectors are in the same bin ($i = j$). An even wider variation is possible when the two vectors are in two different bins i and j . Unfortunately this information is not available in $\bar{T}(k_i, k_j)$ (equation 6) evaluated from the simulation of Mondal et al. (2017). Here we have considered two different assumptions regarding the trispectrum at two different modes \mathbf{k}_1 and \mathbf{k}_2 . These two assumptions correspond to two extreme cases. Case-I: we assume that all the modes within a bin are equally correlated *i.e.* $T(\mathbf{k}_1, -\mathbf{k}_1, \mathbf{k}_2, -\mathbf{k}_2) = T_c(k_i, k_i)$ when \mathbf{k}_1 and \mathbf{k}_2 are both in the i -th bin, and the correlation between modes in two different bins does not depend on the magnitude or orientation of the individual vectors *i.e.* $T(\mathbf{k}_1, -\mathbf{k}_1, \mathbf{k}_2, -\mathbf{k}_2) = T_c(k_i, k_j)$ when \mathbf{k}_1 and \mathbf{k}_2 are in the i -th and j -th bins respectively. Case-II: we assume that the signal in two different Fourier modes is uncorrelated unless $\mathbf{k}_1 = \mathbf{k}_2$ *i.e.* $T(\mathbf{k}_1, -\mathbf{k}_1, \mathbf{k}_2, -\mathbf{k}_2) = \delta_{\mathbf{k}_1, \mathbf{k}_2} T_u(k_i, k_i)$ when the mode \mathbf{k}_i is in the i -th bin. Case-I corresponds to the situation where we have the maximum possible correlation between different modes whereas Case-II corresponds to the situation where we have the minimum possible correlation between two different modes. In reality we expect the correlation between two modes to vary with the separation between the two modes, and the result is expected to lie within the two extreme cases considered here. Considering equation (6), we obtain $T_c(k_i, k_j) = \bar{T}(k_i, k_j)$ for Case-I whereas it predicts $T_u(k_i) = N_{k_i} \bar{T}(k_i, k_i)$ for Case-II. Note that Case-II predicts the error covariance to be completely diagonal with all the off-diagonal terms being zero which is inconsistent with the findings of Mondal et al. (2016). While Case-II is unrealistic for the off-diagonal elements of the covariance matrix, we still consider its predictions for the diagonal elements in order to illustrate the effect of partial decorrelation in the value of the trispectrum across different modes.

We calculate the weights separately for both the cases by extremizing the $\text{SNR} = \bar{P}(k_i) / \sqrt{\mathbf{C}_{ii}}$ with respect to w_g . Considering Case-I the unnormalized weights that extremizes the SNR are

$$\tilde{w}_{gi} = \frac{1}{[\bar{P}(k_i) + P_N(\mathbf{k}_{gi})]^2}, \quad (7)$$

which have $P_N(\mathbf{k}_g)$ in the denominator, *i.e.* the grid points with higher noise contribute less to the bin averaged quantities. The grid points \mathbf{k}_g which are unsampled during observations, *i.e.* $\tau(\mathbf{k}_g) = 0$, have $P_N(\mathbf{k}_g) = \infty$ (equation 1). The weight $\tilde{w}_g = 0$ (equation 7) for the unsampled grid points and they do not contribute to the bin averaged quantities. Using equation (7) in equation (4) we obtain the corresponding PS error covariance matrix

$$\mathbf{C}_{ij} = \frac{1}{\sum_{g_i} \tilde{w}_{gi}} \delta_{ij} + \frac{\bar{T}(k_i, k_j)}{V}. \quad (8)$$

For comparison we consider the error covariance for a situation where the signal is a Gaussian random field for which the trispectrum is zero. The weights \tilde{w}_{gi} here are unchanged and these are given by equation (7), and we have the PS error covariance matrix

$$\mathbf{C}_{ij}^G = \frac{1}{\sum_{g_i} \tilde{w}_{gi}} \delta_{ij}. \quad (9)$$

The diagonal terms of the covariance matrices (equations 8 and 9) predicts the error variance in the measured EoR 21-cm PS, *i.e.* $\mathbf{C}_{ii} = \langle [\Delta \hat{P}(k_i)]^2 \rangle$. Equations (8) and (9) indicate that the Gaussian consideration underestimates the variance of the measured PS. The off-diagonal terms of the covariance matrix ($i \neq j$) predict the correlation between the errors at the i -th and j -th bins $\mathbf{C}_{ij} = \langle [\Delta \hat{P}(k_i) \Delta \hat{P}(k_j)] \rangle$. The off-diagonal terms are zero for a Gaussian random field, and the errors in the different bins are uncor-

related. Non-Gaussianity however may introduce correlations between the different bins through the off-diagonal components of the trispectrum.

We first discuss the diagonal terms \mathbf{C}_{ii} , *i.e.* the variance. This has contributions from the cosmic variance as well as the system noise. The noise PS $P_N(\mathbf{k}_{gi})$ scales as t_{obs}^{-1} (equation 1) and this has a large value for small observation times. Considering the behaviour of \mathbf{C}_{ii} , for small observation times this is governed by the system noise contribution and we have

$$\mathbf{C}_{ii} \simeq \left(\frac{8 \text{ hrs}}{t_{\text{obs}}} \right)^2 \times \frac{P_0^2}{\sum_{g_i} [\tau(\mathbf{k}_{gi})]^2}. \quad (10)$$

Equation (10) shows that $\mathbf{C}_{ii} \propto t_{\text{obs}}^{-2}$ and consequently $\text{SNR} \propto t_{\text{obs}}$ for small observation times. The observations with very large t_{obs} elucidate another extreme of the error estimates (equation 8) where $P_N(\mathbf{k}_g) \simeq 0$, and \mathbf{C}_{ii} converges to the ‘‘cosmic variance’’ which is given by

$$\mathbf{C}_{ii} = \frac{\bar{P}^2(k_i)}{N_{g_i}} + \frac{\bar{T}(k_i, k_i)}{V}. \quad (11)$$

where N_{g_i} is the number of sampled grid points in the i -th bin. The cosmic variance represents the lower limit for the PS error variance. This arises due to the inherent statistical uncertainty in the EoR 21-cm signal. The actual predicted error variance for a finite observing time will typically be larger than this due to the system noise contribution.

The corresponding cosmic variance for a Gaussian random field (equation 9) is given by

$$\mathbf{C}_{ii} = \frac{\bar{P}^2(k_i)}{N_{g_i}}. \quad (12)$$

A comparison of equations (11) and (12) illustrates an important difference between the Gaussian and non-Gaussian situations. We see that it is possible to reduce the cosmic variance with no lower bound by combining the signal from a larger number of \mathbf{k} modes in the bin *i.e.* increasing N_{g_i} . In contrast, the presence of the trispectrum in equation (11) sets a lower limit to the value of \mathbf{C}_{ii} , and it is not possible to lower the variance any further by increasing the number of \mathbf{k} modes (Mondal et al. 2015).

Next considering the off-diagonal terms $\mathbf{C}_{ij} = \bar{T}(k_i, k_j)/V$ (equation 8) which quantify the correlation between different bins, we see that this only depends on the trispectrum. This is intrinsic to the signal, and therefore is independent of the system noise and observation time.

Considering Case-II, the unnormalized weights are given by

$$\tilde{w}_{gi} = \frac{1}{[\bar{P}(k_i) + P_N(\mathbf{k}_{gi})]^2 + N_{k_i} V^{-1} \bar{T}(k_i, k_i)}, \quad (13)$$

which differ from the weight in Case-I (equation 7). The weights now include a contribution from the trispectra for the non-Gaussian signal. Here also the weights are zero for the grid points which are not sampled by the baseline distribution. The weights for Case-II match those for Case-I (equation 7) if the signal were a Gaussian random field. The PS error covariance (using equations 4 and 13) in Case-II is given by

$$\mathbf{C}_{ij} = \frac{1}{\sum_{g_i} \tilde{w}_{gi}} \delta_{ij}. \quad (14)$$

Note that Case-II does not take into account the correlation between the different \mathbf{k} grid points which makes the off-diagonal terms of the covariance matrix to be zero. The error covariance \mathbf{C}_{ii} for Cases I and II match for small observation times, and they have

very similar forms for very long observation times (cosmic variance) where for Case–II we have

$$\mathbf{C}_{ii} = \frac{\bar{P}^2(k_i)}{N_{gi}} + \frac{N_{k_i}}{N_{gi}} \frac{\bar{T}(k_i, k_i)}{V}. \quad (15)$$

This differs from the predictions for Case–I (equation 11) by the factor $f = N_{k_i}/N_{gi}$ which appears in equation (15). In our analysis we find that f has values in the range $0.1 \leq f \leq 0.3$ for $k < 3 \text{ Mpc}^{-1}$ and $f \leq 1.0$ over the rest of the k range considered here. We see that the error predictions for Case–II are smaller than those for Case–I. The error predictions for Case–II are expected to lie somewhere in between the Gaussian predictions and Case–I which assumes that all the k modes in a bin are equally correlated.

We have used the resulting covariance matrices (equations 8, 9 and 14) to predict the errors for PS measurements in the different redshift slices introduced earlier in this section.

4 RESULTS

Figure 1 shows the dimensionless EoR 21-cm PS $\Delta_b^2(k) = k^3 \bar{P}(k)/2\pi^2$ (solid purple line) and the corresponding 5σ error estimates for Case–I. The solid lines represent the non-Gaussian error predictions $E_b(k) = 5 \times \sqrt{\mathbf{C}_{ii}}$ (equations 8) and the dashed lines represent the corresponding Gaussian error predictions $E_{bG}(k)$ (equation 9), both of these have been multiplied with $k^3/2\pi^2$ to make them dimensionless. The error estimates have contributions from both the cosmic variance and the system noise. There are broadly two main features visible in Figure 1. (1.) We see that the system noise contribution dominates the errors at large k . These errors come down as t_{obs} is increased. The errors also come down at lower z where the system noise contribution is smaller (T_{sky} increases with redshift). For each t_{obs} and z we can identify a largest mode (k_m) below which ($k \leq k_m$) a 5σ detection of the 21-cm power spectrum will be possible. A larger k range becomes accessible for a 5σ detection (k_m increases) as t_{obs} is increased or we move to a lower z . This is studied in more detail in Figure 2 which we discuss later. (2.) We see noticeable differences between $E_b(k)$ and $E_{bG}(k)$. These differences are most prominent for the cosmic variance (CV) predictions which corresponds to the limit $t_{\text{obs}} \rightarrow \infty$ where the system noise becomes insignificant. The system noise contribution is inherently Gaussian whereas the 21-cm signal is non-Gaussian. We find that the values of $E_b(k)$ and $E_{bG}(k)$ match for small t_{obs} when the system noise dominates the errors. The differences between $E_b(k)$ and $E_{bG}(k)$ become noticeable as t_{obs} is increased. The differences are primarily noticeable at small k where there is a relatively smaller system noise contribution as compared to large k . The differences also become more pronounced as we move to lower z where there is a smaller system noise contribution. The differences between $E_b(k)$ and $E_{bG}(k)$ are studied in detail in Figure 3 which we discuss later.

Considering Figure 1, we see that the predicted error estimates $E_b(k)$ all increase with k mainly due to the system noise contribution in contrast to the expected signal $\Delta_b^2(k)$ which is relatively flat across the relevant k range. This implies that for any given t_{obs} a detection of the signal will only be possible at small k whereas the errors in the power spectrum will dominate at large k . Figure 2 shows the largest k mode k_m , below which SKA-Low will be able to measure the EoR 21-cm PS at $\geq 5\sigma$ confidence. We show this as a function of z for the four representative values of t_{obs} indicated in the figure. We see that the value of k_m increases as z decreases *i.e.* for a fixed observation time, we will progressively be able to probe a

larger range of length-scales as reionization progresses. This is primarily a consequence of the fact that the system noise comes down at lower z , further the amplitude of the 21-cm PS also increases as reionization progresses. However the amplitude peaks at $\sim 50\%$ reionization and drops beyond this, causing k_m to fall at $z = 7$. Considering $t_{\text{obs}} = 128 \text{ hrs}$ we find that there is a limited k range across which a 5σ detection of the 21-cm PS is possible. This is restricted to $k \leq 0.2 \text{ Mpc}^{-1}$ at high z ($= 11, 13$) and increases somewhat to $k \leq 0.8 \text{ Mpc}^{-1}$ at $z = 7$ and 8. There is a significant increase in the values of k_m (by a factor of $\sim 2.5 - 5$) if t_{obs} is increased to 1,024 hrs. We see that with $t_{\text{obs}} = 1,024 \text{ hrs}$ a 5σ detection will be possible in the range $k \leq 1 \text{ Mpc}^{-1}$ at $z \leq 11$. The value of k_m increases gradually if t_{obs} is increased beyond 1,024 hrs. However, we see an exception at $z = 13$ where there is a significant increase in k_m if t_{obs} is increased beyond 1,024 hrs. The values of k_m increase very slowly for $t_{\text{obs}} \geq 10,000 \text{ hrs}$ and k_m values are in the range $2 - 4 \text{ Mpc}^{-1}$ for $t_{\text{obs}} = 50,000 \text{ hrs}$.

Figure 3 shows the deviation $\Delta = (E_b - E_{bG})/E_{bG}$ of the non-Gaussian error estimates with respect to the corresponding Gaussian estimates. These deviations arise due to the contribution from the trispectrum (equation 8). Earlier studies (Mondal et al. 2016, 2017) show that the trispectrum increases at larger k (smaller length-scales), and it also increases as reionization proceeds *i.e.* z decreases. These effects are reflected in the behaviour of the cosmic variance (CV), which ignores the system noise. Considering the CV, we see that the deviations are minimum at around $k_{\text{min}} \sim 0.1 - 0.3 \text{ Mpc}^{-1}$, and the deviations increase monotonically at both smaller and larger k values. At the smallest k bin (0.04 Mpc^{-1}) we find $\Delta \geq 100\%$ at $z = 7$ and 9, whereas $\Delta \sim 20\%$ to 50% for the other redshifts. The values of Δ increase significantly at $k > k_{\text{min}}$ with deviations of order $\sim 100\%$ or larger at $k \approx 4 \text{ Mpc}^{-1}$ for the entire z range. Considering the redshift evolution of CV, we see that at large k the deviations from the Gaussian predictions increase as reionization proceeds.

We see that for $k < k_{\text{min}}$ the values of Δ approach the CV limit within $t_{\text{obs}} = 1,024 \text{ hrs}$ for $z \geq 9$ and within $t_{\text{obs}} = 128 \text{ hrs}$ for lower redshifts. We find the bins at $k > k_{\text{min}}$ are largely system noise dominated, and the deviations at these bins are small for $z \leq 9$ even for an observing time of 50,000 hrs. However, at $z = 8$ we find that Δ also increases at large k ($> k_{\text{min}}$) for $t_{\text{obs}} \geq 10,000 \text{ hrs}$ and we have $\Delta \sim 40\%$ at $k \sim 0.5 \text{ Mpc}^{-1}$ for $t_{\text{obs}} = 50,000 \text{ hrs}$. These deviations increase significantly at $z = 7$ where $\Delta \geq 100\%$ at $k \sim 0.2 - 0.5 \text{ Mpc}^{-1}$ for $t_{\text{obs}} = 1,024 \text{ hrs}$. The k range where $\Delta \geq 100\%$ increases further to $k \sim 0.2 - 1 \text{ Mpc}^{-1}$ if t_{obs} is increased further to 10,000 hrs.

We next consider how the SNR for the 21-cm PS grows with increasing observation time t_{obs} . Figures 4, 5 and 6 show the results for three representative k bins located at 0.04 Mpc^{-1} (large scales), 0.57 Mpc^{-1} (intermediate scales) and 1.63 Mpc^{-1} (small scales) respectively. The SNR values are shown for both Case–I (purple solid line) and Case–II (blue solid line), as well as the Gaussian predictions (dotted black line). The cosmic variance (CV) limits ($t_{\text{obs}} \rightarrow \infty$) are shown as shaded regions for both the non-Gaussian (Case–I) and Gaussian predictions. We find that the differences between Case–I, II and the Gaussian predictions are noticeable only when the SNR approaches the cosmic variance limit. The Gaussian predictions are the most optimistic of the three, and the SNR values for Case–II are typically between those for Case–I and the Gaussian predictions. The figure also shows how Δ increases with t_{obs} at the specified values of k .

Considering the lowest k bin ($k = 0.04 \text{ Mpc}^{-1}$, Figure 4), the SNR is largely constrained by the cosmic variance with a relatively

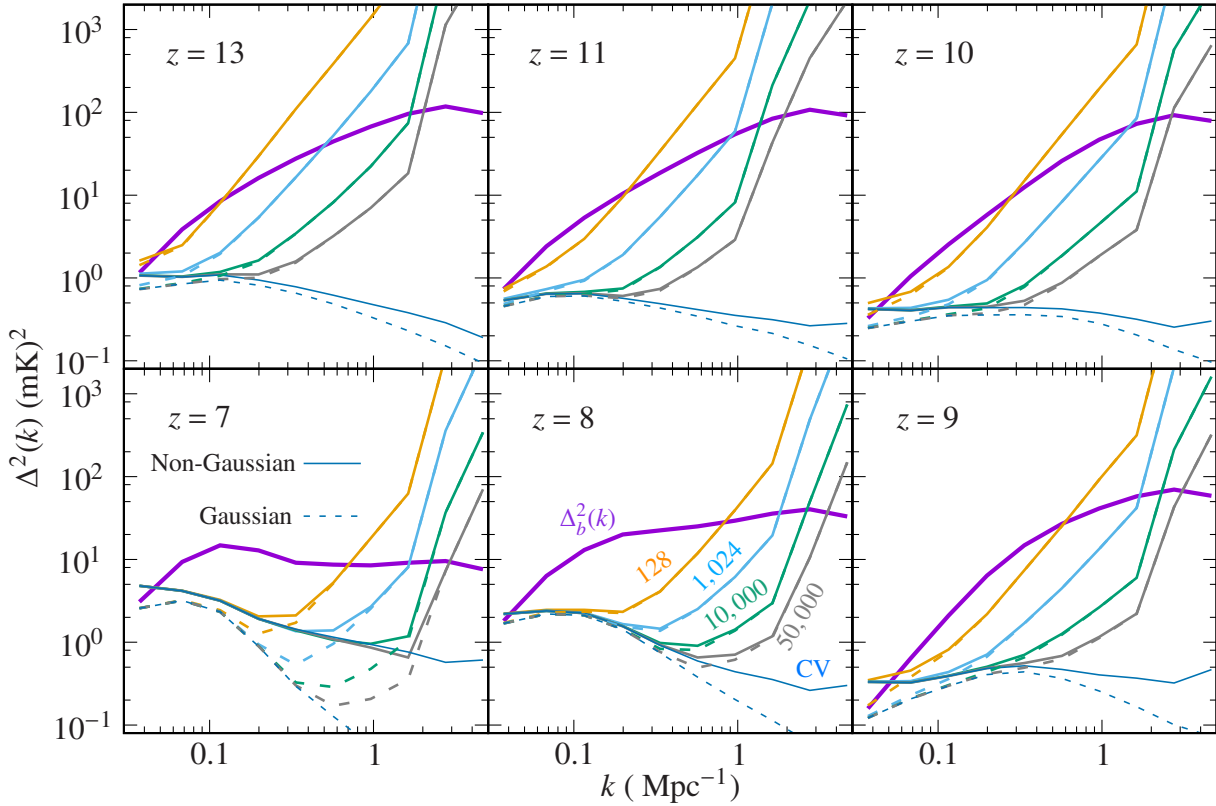


Figure 1. This shows the mean squared 21-cm brightness temperature fluctuations $\Delta_b^2(k)$ and the corresponding 5σ error estimates for different t_{obs} for six different redshifts considering Case-I. The solid lines represent the non-Gaussian errors and the dashed lines represent the corresponding Gaussian errors. We also show the cosmic variance which is the lowest limit of the error estimates (thin lines).

small system noise contribution. The SNR saturates to the cosmic variance limit within a few hundred hours of observations at $z \leq 10$ and within $t_{\text{obs}} \sim 3,000$ hrs for $z > 10$. Considering Case-I, a $\geq 5\sigma$ measurement of the EoR 21-cm PS will be possible with $t_{\text{obs}} \geq 128$ hrs at redshifts $z = 13, 11, 8$ and with $t_{\text{obs}} \geq 3,000$ hrs at $z = 10$, whereas a 5σ detection is limited by the cosmic variance at $z = 7$ and 9. However, the Case-II predictions are more optimistic and they predict a 5σ detection to be possible. The deviations between the non-Gaussian and Gaussian predictions are found to become important ($\Delta \geq 50\%$) within a few hundred hours of observations at redshifts $z = 10, 9$ and 7.

Considering $k = 0.57 \text{ Mpc}^{-1}$ (Figure 5), the limiting SNR (CV) increases to values > 100 at $z \geq 8$ and ~ 40 at $z = 7$ implying that a high precision measurement of the EoR 21-cm PS is possible at these length-scales provided that t_{obs} is adequately large. The t_{obs} needed for a 5σ detection is $\sim 1,000$ hrs at $z = 13$ and it comes down at lower z to ~ 128 hrs at $z = 8$ and 7. The SNR is highest at $z = 8$ and we have $\text{SNR} \approx 100$ in $\sim 4,000$ hrs of observations. The non-Gaussian effects make a relatively small contribution to the error predictions at this length-scale with $\Delta \leq 20\%$ in the range $z \geq 8$ for $t_{\text{obs}} \leq 10^4$ hrs. The non-Gaussian effects increase somewhat at $z = 7$ where we have $\Delta \approx 250\%$ for $t_{\text{obs}} \approx 10^4$ hrs.

Considering the bin at $k = 1.63 \text{ Mpc}^{-1}$ (Figure 6) the SNR is largely system noise dominated. The SNR is well below the cosmic variance limit and increases with t_{obs} for the range shown

in the figure except for the Case-I at $z = 7$. A 5σ detection will be possible with $t_{\text{obs}} \approx 20000, 40000, 2000, 1000$ and 600 hrs at $z = 13, 11, 10, 9$, and 8 respectively. The value of the 21-cm PS falls at $z = 7$ and the minimum observation time required for a 5σ detection increases to 1,000 hrs. The inherent non-Gaussianity of the 21-cm signal is important only at $z = 7$ where we have $10\% \leq \Delta \leq 100\%$ for $10^4 \text{ hrs} \leq t_{\text{obs}} < 10^5 \text{ hrs}$.

We now discuss the off-diagonal elements of the covariance matrix \mathbf{C}_{ij} which is a measure of the correlation between error estimates at different k bins. The off-diagonal terms of the covariance \mathbf{C}_{ij} do not change with the observation time as we see in equation (8). It is convenient to consider the dimensionless correlation coefficients $r_{ij} = \mathbf{C}_{ij} / \sqrt{\mathbf{C}_{ii}\mathbf{C}_{jj}}$. The value $r_{ij} = 1$ indicates a perfect correlation between the errors at the two bins, whereas $r_{ij} = -1$ implies a complete anti-correlation. The errors in the two bins are completely uncorrelated if $r_{ij} = 0$ i.e. the two PS measurements are independent. Values $r_{ij} > 0$ and $r_{ij} < 0$ indicate partial correlation and anti-correlation respectively. An earlier work (Mondal et al. 2017) presents a detailed analysis of the correlations r_{ij} evaluated from simulations. It was found that the non-Gaussianity inherent in the EoR 21-cm signal introduces a complex pattern of correlations and anti-correlations between the different k bins. It was further found that these correlations (and anti-correlations) were statistically significant i.e. they were in excess of the statistical fluctuations expected if the signal were purely a Gaussian random field. However,

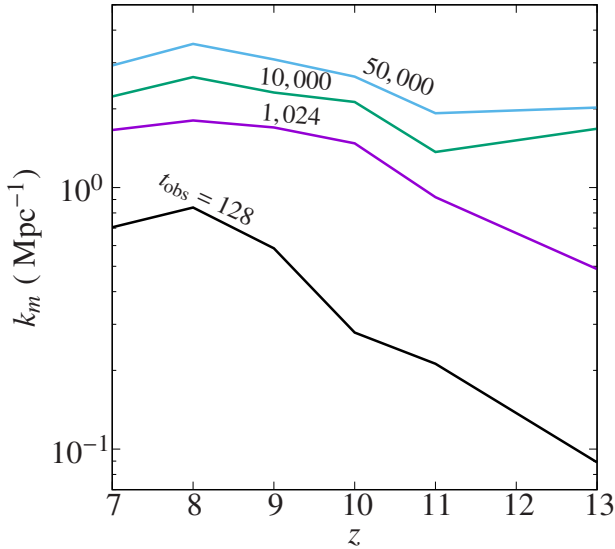


Figure 2. This shows the variation of the maximum Fourier mode k_m which will be detected at a 5σ level as a function of z for the four t_{obs} indicated in the figure.

the earlier work did not include the effects of the baseline sampling and system noise corresponding to observations with a radio-interferometric array. For an array like SKA-Low the correlation coefficient r_{ij} is dependent on the observation time through the diagonal elements \mathbf{C}_{ii} which appear in the denominator. As discussed earlier, the values of \mathbf{C}_{ii} are typically large for small t_{obs} where they are system noise dominated. The relative significance of the correlations between the errors in different k bins is small for small t_{obs} where r_{ij} has small values. The relative significance of these correlations increase as \mathbf{C}_{ii} approaches the cosmic variance and we have considered $t_{\text{obs}} = 1,024$ hrs for our analysis. The values of r_{ij} will increase if we consider a larger observation time.

Considering Figure 7, we see that in addition to $r_{ii} = 1$ (by definition) for all the diagonal elements, we have both positive and negative values of r_{ij} . The redshifts $z = 13, 11$ and 10 show very similar features with a positive correlation ($r_{ij} \sim 0.1$ to 0.3) between the two smallest k bins ($0.04, 0.07 \text{ Mpc}^{-1}$), and the third bin (0.12 Mpc^{-1}) is anti-correlated ($r_{ij} \sim -0.4$ to -0.1) with the two smaller k bins and one larger k bin (0.20 Mpc^{-1}). The nature of these correlations changes at $z = 9$ where the first five k bins ($k \leq 0.34 \text{ Mpc}^{-1}$) are correlated. Of these, the four largest k bins are strongly correlated ($0.2 \leq r_{ij} < 0.7$) among themselves whereas the smallest k bin is only mildly correlated ($r_{ij} < 0.2$) with the other bins. At $z = 8$, the first three k bins are correlated ($r_{ij} \leq 0.3$) whereas the fifth bin shows anti-correlations ($r_{ij} > -0.3$) with the second and third bins. Considering $z = 7$, the first two k bins are anti-correlated ($r_{ij} \geq -0.3$) with the other bins while the next five k bins show strong correlations ($0.15 \leq r_{ij} \leq 0.85$). We thus see that there are noticeable correlations and anti-correlations between the errors in the estimated 21-cm PS in different k bins at all stages of reionization. These correlations span a wide range of k modes depending on the redshift.

5 EFFECTS OF FOREGROUNDS

Foregrounds, which are almost 4–5 order magnitude larger than the EoR 21-cm signal (e.g. Ghosh et al. 2012), are a ma-

jor challenge for measuring the EoR 21-cm PS. There are several approaches which have been proposed to handle the foreground problem, one of these being foreground removal (e.g. Morales et al. 2006; Ali et al. 2008; Harker et al. 2009; Parsons et al. 2012; Bonaldi & Brown 2015; Chapman et al. 2015; Pober et al. 2016b). The entire analysis till now has assumed that the foregrounds have been perfectly modelled and removed, following Chatterjee & Bharadwaj (2018) we refer to this as the “Optimistic” scenario in the subsequent discussion.

The foreground contribution to the 21-cm PS is predicted to be localized within a wedge in the $(k_{\perp}, k_{\parallel})$ plane (Datta et al. 2010), the boundary of this wedge being defined through (Morales et al. 2012)

$$k_{\parallel} = \left[\frac{r_c \sin(\theta_L)}{r'_c v_c} \right] k_{\perp} \quad (16)$$

where θ_L is the maximum angular position in the sky (relative to the telescope pointing) from which foregrounds contaminate the signal. The $k(k_{\perp}, k_{\parallel})$ modes outside this foreground wedge are expected to be free of foreground contamination, and the “foreground avoidance” technique (e.g. Pober et al. 2013; Kerrigan et al. 2018) proposes to utilize only these modes to estimate the EoR 21-cm PS. Typically $\theta_L = 90^\circ$ corresponding to the horizon which is the maximum angle from which the foregrounds contaminate the signal. However it is possible to taper the telescope’s field of view (Ghosh et al. 2011; Choudhuri et al. 2016a) and thereby restrict θ_L to an angle smaller than the horizon. Here in addition to $\theta_L = 90^\circ$ we also consider a situation where we assume that tapering is used whereby $\theta_L = 3 \times \text{FWHM}/2$ where FWHM is the Full Width Half Maxima of the SKA-Low primary beam. Note that FWHM changes with frequency and it is $\sim 6^\circ$ at $z = 8$. Following Chatterjee & Bharadwaj (2018), we refer to the two cases $\theta_L = 3 \times \text{FWHM}/2$ and 90° as the “Moderate” and “Pessimistic” scenarios respectively.

Figure 8 shows the SNR for detecting the EoR 21-cm PS at different k bins for various z values considering the non-Gaussian error covariance for Case-I. Starting from the left the three columns show the predictions for the Optimistic, Moderate and Pessimistic scenarios respectively while the upper and lower rows corresponds to $t_{\text{obs}} = 1,024$ and $10,000$ hrs respectively. The first point to note is that a few k bins for which all the k modes are within the foreground wedge are excluded from the detection of the EoR 21-cm PS. These excluded k bins occur at the two extremities (large k and small k). Further in equation (16) the factor $r_c/(r'_c v_c) \sim \sqrt{1+z}$ causes the extent of the foreground wedge to increase with z (θ_L also increases with z in the Moderate scenario) and we see that the extent of the excluded k bins increases at higher redshifts.

In each k bin the number of k modes which can be used for measuring the 21-cm PS decreases from the Optimistic to the Moderate and then the Pessimistic scenarios. This causes the SNR to decrease from the Optimistic to the Moderate scenario, and the SNR decreases even further for the Pessimistic scenario. The k range where the SNR exceeds 5 does not change very much from the Optimistic to Moderate scenario for both 1,024 and 10,000 hrs, except for a small raising of the lower k limit. The lower k limit for a 5σ detection increases significantly for the Pessimistic scenario, however the upper k limit is not much affected outside the excluded bins. In all cases the SNR peaks at $z = 8$. Considering the region where the SNR exceed 30 we see that for the Optimistic scenario with 1,024 hrs this spans from $z = 7$ to 10 and $k = 0.1 \text{ Mpc}^{-1}$ to 0.8 Mpc^{-1} . The range shrinks to $z = 7-9$ and $k = 0.2-0.8 \text{ Mpc}^{-1}$ for the Moderate scenario and shrinks even further to a very small

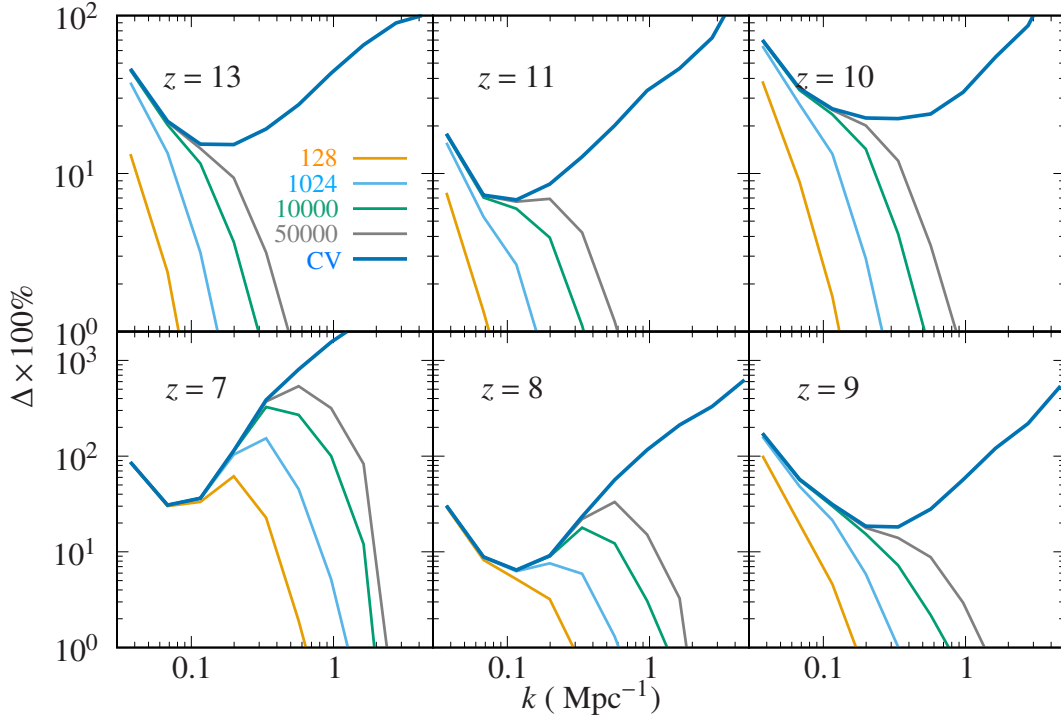


Figure 3. This shows the % deviation of $E_b(k)$ with respect to the Gaussian predictions $E_{bG}(k)$ considering Case-I.

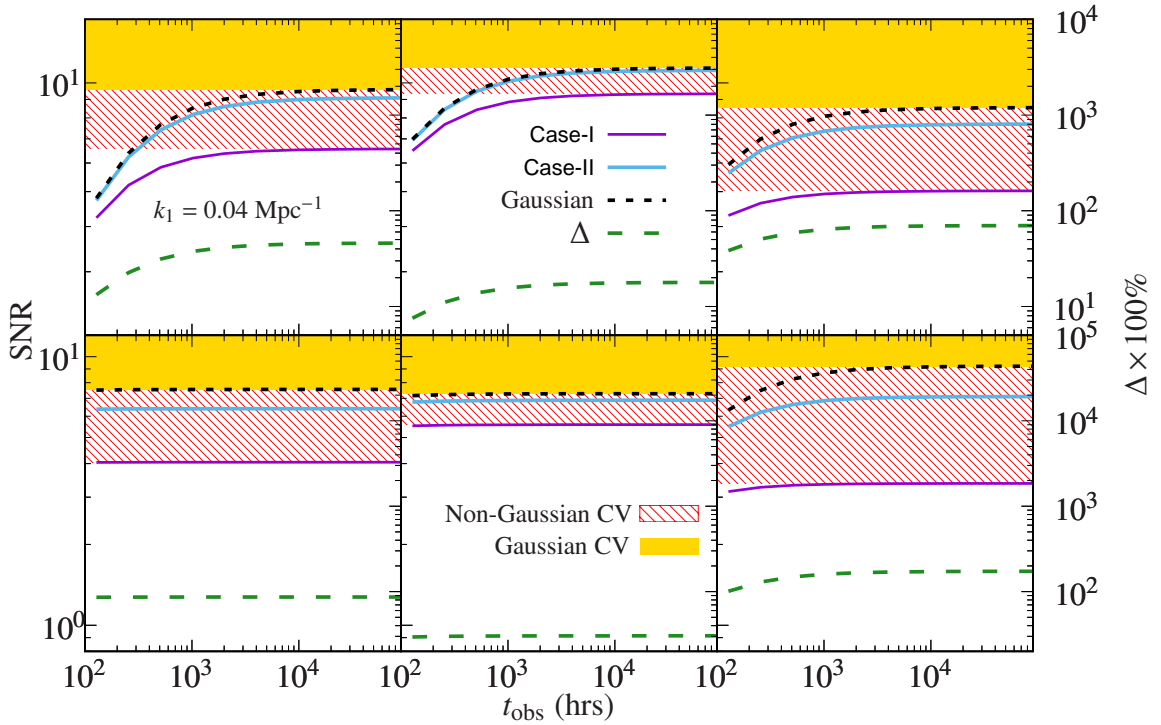


Figure 4. This shows the SNR (left axis) as a function of the observing time t_{obs} for $k = 0.04 \text{ Mpc}^{-1}$ which is representative of large length-scales. Results are shown for Case-I, Case-II and the Gaussian predictions, while the two shaded regions demarcate the cosmic variance limits for Case-I and the Gaussian predictions respectively. The dashed line (green) shows Δ (right axis) as a function of t_{obs} . The different panels, each of which corresponds to a different redshift, are arranged the same way as in Figure 3.

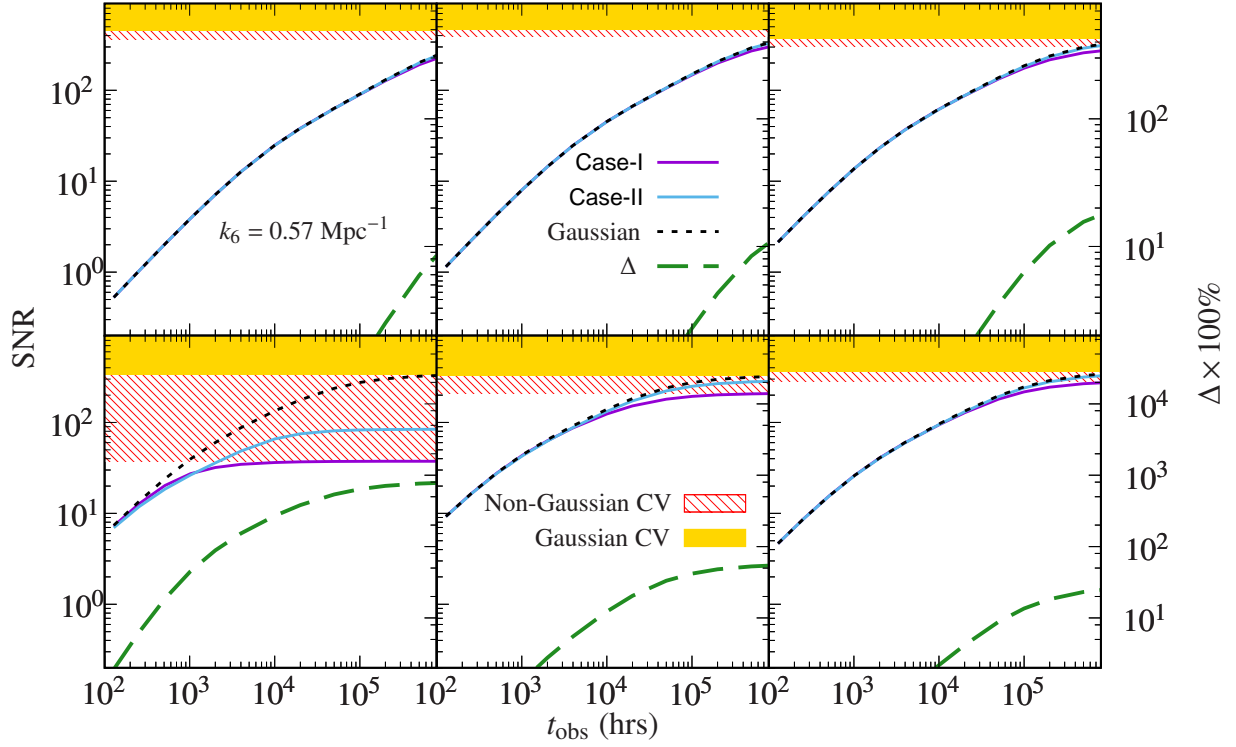


Figure 5. Same as Figure 4 for $k = 0.57 \text{ Mpc}^{-1}$.

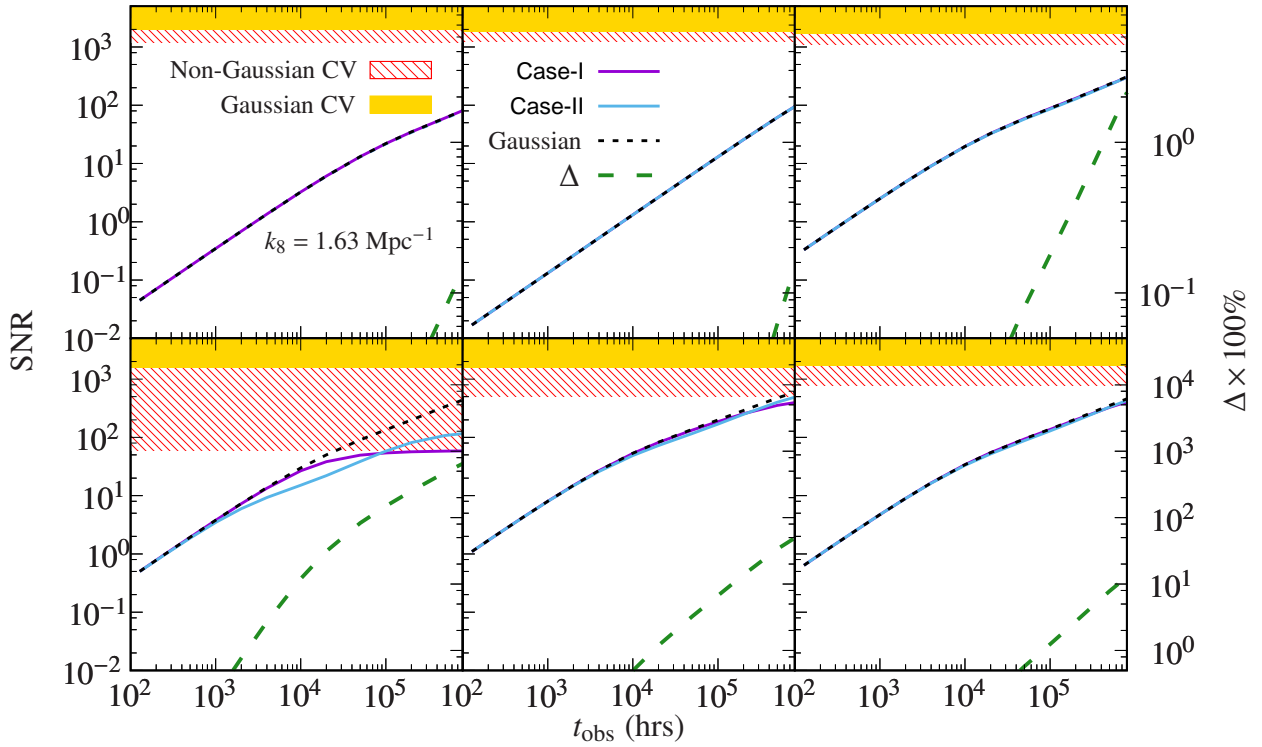


Figure 6. Same as Figure 4 for $k = 1.63 \text{ Mpc}^{-1}$.

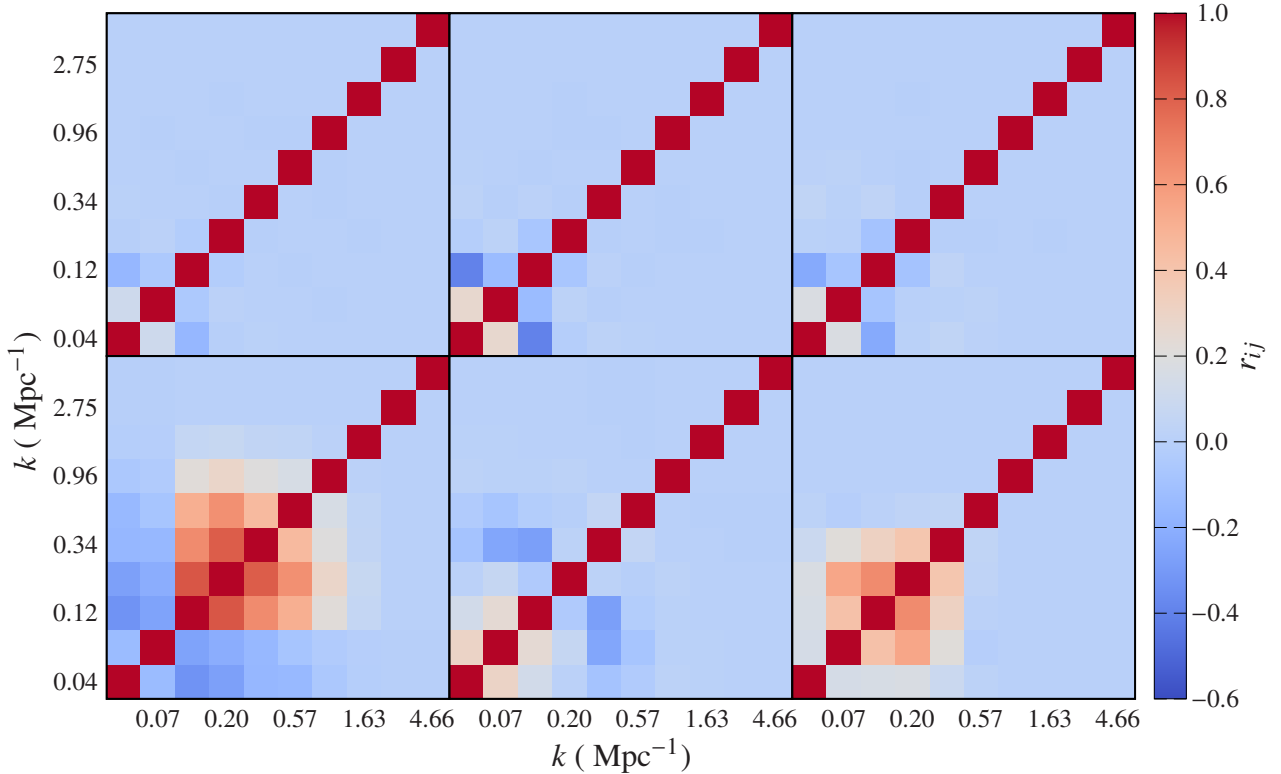


Figure 7. This shows the correlation coefficient r_{ij} for the errors at different k bins for 1,024 hrs of observations. The different panels, each of which corresponds to a different redshift, are arranged the same way as in Figure 3.

region around $z = 8$ and $k = 0.6 \text{ Mpc}^{-1}$ for the Pessimistic scenario. The range where the SNR exceeds 30 increases significantly if the observing time is increased to 10,000 hrs, this is particularly prominent for the Pessimistic scenario where both the z and k ranges are considerably increased compared to 1,024 hrs.

Figure 9 shows the percentage deviation Δ of the non-Gaussian error predictions (Case-I) with respect to the Gaussian predictions. Considering the Optimistic scenario discussed in the previous section (Figure 3), the deviations are prominent ($\Delta > 50\%$) at the smallest k bin for $z = 7$ and 9 and also in the k range $0.2 - 0.5 \text{ Mpc}^{-1}$ at $z = 7$. The number of k modes in each k bin gets reduced due to the foreground wedge, and consequently the relative contribution to the error covariance (equation 11) from the trispectrum is reduced. We therefore expect progressively smaller values of Δ as we go from the Optimistic to the Moderate and the Pessimistic scenarios. Considering the Moderate scenario, the results are similar to the Optimistic ones, however the values of Δ are somewhat smaller though they still exceed 50% (and 100% in some cases). For the Pessimistic scenario, however, the values of Δ are considerably smaller and they do not exceed 50% for 1,024 hrs whereas they exceed 50% only in the k range $0.3 - 1 \text{ Mpc}^{-1}$ at $z = 7$ for 10,000 hrs.

Figure 10 shows the correlations between the different k bins induced by the non-Gaussianity considering 10,000 hrs. We have restricted the analysis to $z = 7$ where we have prominent deviations from the Gaussian predictions for all the three scenarios. Comparing the Optimistic scenario with the lower left panel of Figure 7 which shows the same for $t_{\text{obs}} = 1,024$ hrs we find that the extent

of the positive correlation increases by one k bin and the values of the correlation coefficients r_{ij} also increase. Comparing the left and center panels of Figure 10 we see that the pattern of correlations and anti-correlations has the same k extent for the Optimistic and Moderate scenarios, however the magnitudes of r_{ij} decrease by 10 – 30%. Considering the Pessimistic scenario, we find that the anti-correlation between the two smallest k bins and the larger k bins is not noticeable here. The extent of the k bins with positive correlations is the same as the Optimistic scenario but the values of r_{ij} are 60 – 70% smaller. Considering other redshifts for which the results are not shown here we find that there are some correlations between the different k bins also at $z = 9$ in the Moderate scenario, however these are absent in the Pessimistic scenario. These correlations for the Moderate scenario are however considerably smaller and they are $\sim 50\%$ of the correlations seen in the bottom-right panel of Figure 7.

Summarizing this section we find that foregrounds restrict the k modes which can be used for detecting the EoR 21-cm PS. This results in reducing the SNR and also reducing the impact of non-Gaussianity on the error predictions. The deviations from the Gaussian predictions continue to be important ($> 50\%$) at $z = 7$ even if the effect of Foreground Avoidance is included.

6 SUMMARY AND CONCLUSIONS

There are currently several radio-interferometric arrays such as LOFAR, MWA and PAPER which have been carrying out observations to detect the EoR 21-cm PS. Several other instruments like

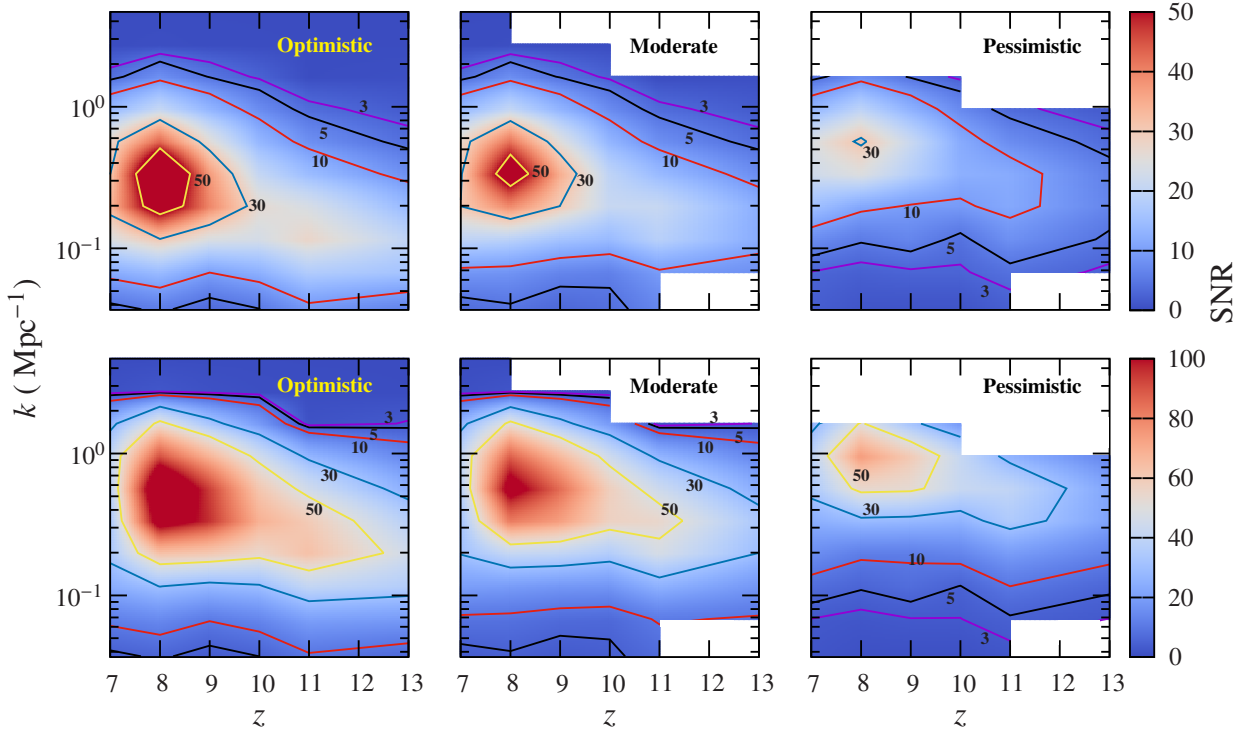


Figure 8. This shows the predicted SNR (non-Gaussian Case-I) as a function of k and z for the three different foreground scenarios. The top and bottom panels show the results for 1,024 hrs and 10,000 hrs of observations respectively. Note that the color bars are different for the top and bottom panels.

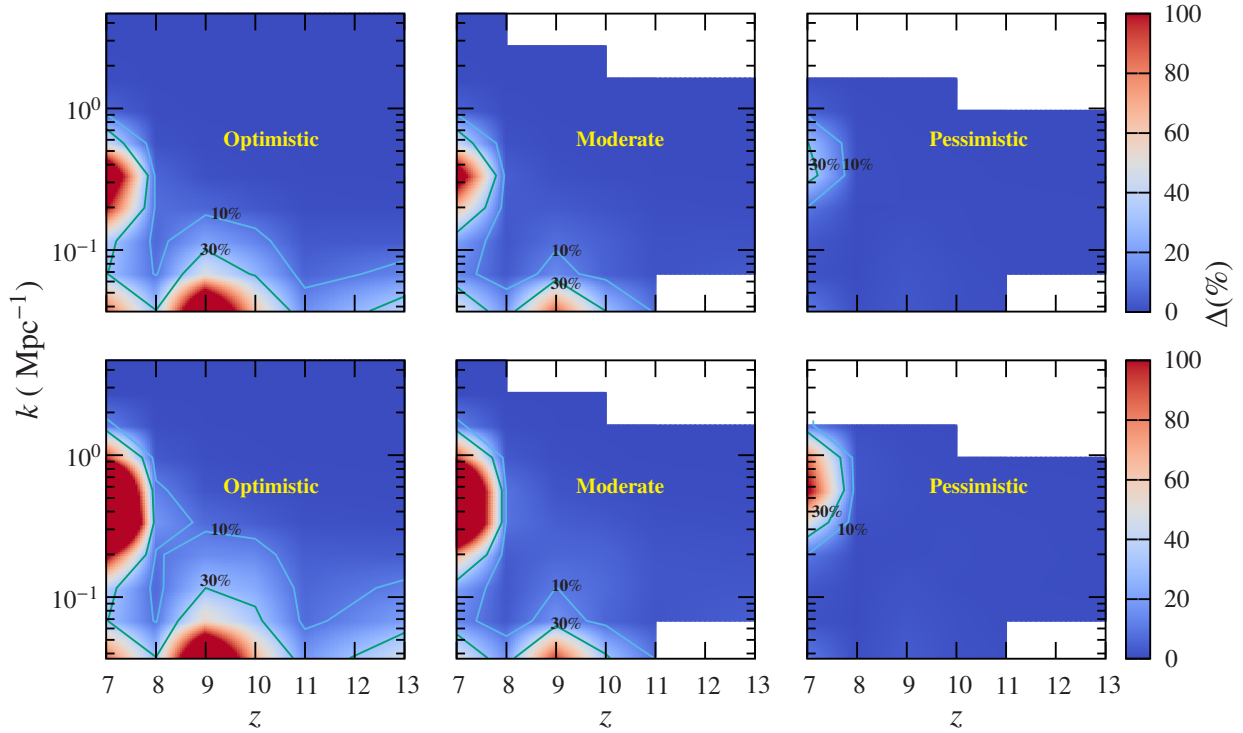


Figure 9. This shows Δ the percentage deviation of the non-Gaussian (Case-I) error predictions from the Gaussian predictions as a function of k and z considering the three different foreground scenarios. The top and bottom panels show the results for 1,024 hrs and 10,000 hrs of observations respectively.

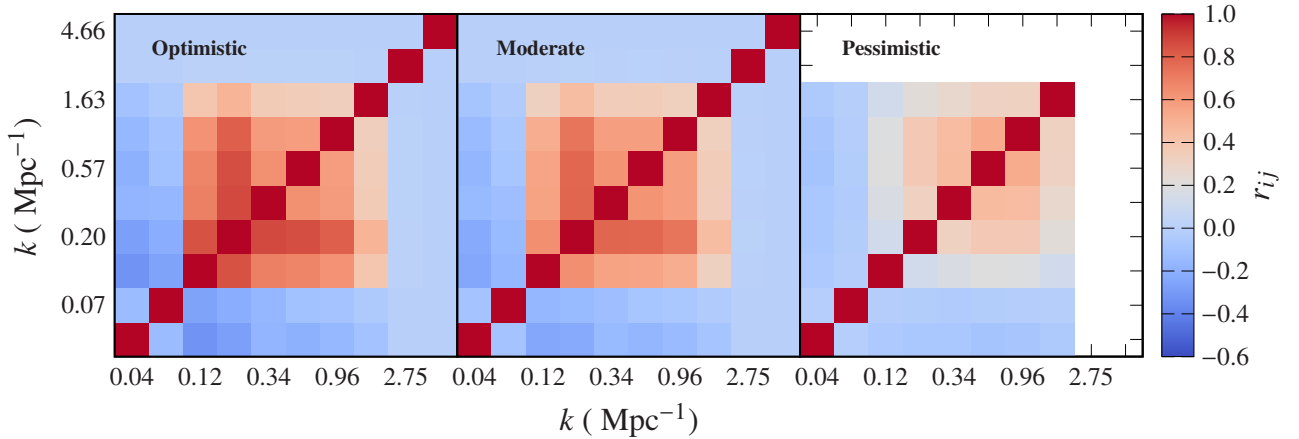


Figure 10. This shows the correlation coefficients r_{ij} at $z = 7$ considering the three different foreground scenarios for $t_{\text{obs}} = 10,000$ hrs. In the Pessimistic scenario the two largest k bins are excluded due to the Foreground wedge.

HERA and SKA, which are expected to have greater sensitivity, are under construction or planning. It is of considerable interest to have error predictions for the EoR 21-cm PS considering such observations, and there have been several works (e.g. Mellema et al. 2013; Poher et al. 2014; Greig & Mesinger 2015; Ewall-Wice et al. 2016) addressing this under the assumption that the EoR 21-cm signal is a Gaussian random field. However there have been several studies (e.g. Bharadwaj & Pandey 2005; Mondal et al. 2015, 2016, 2017; Majumdar et al. 2018) which show that the EoR 21-cm signal is non-Gaussian in nature. In this paper we study how these non-Gaussianities affect the error estimates for the EoR 21-cm PS considering observations with the upcoming SKA-Low.

The error predictions for any observation of the EoR 21-cm PS are quantified through the error covariance matrix \mathbf{C}_{ij} which depends on the PS and the trispectrum of the EoR 21-cm signal, and also observational effects like the array baseline distribution and the system noise. The EoR simulations generally provide predictions for the bin-averaged 21-cm PS and trispectrum without incorporating the observational effects. In this paper we first present a methodology for calculating \mathbf{C}_{ij} combining the simulated PS and trispectrum with these observational effects. The error covariance matrix for the binned 21-cm PS (equation 4) actually depends on the trispectrum $T(\mathbf{k}_{g_i}, -\mathbf{k}_{g_i}, \mathbf{k}_{g_j}, -\mathbf{k}_{g_j})$ evaluated at individual pairs of Fourier modes \mathbf{k}_{g_i} and \mathbf{k}_{g_j} , unfortunately this is not available from simulations as the computations involved for a reliable estimate is extremely large and cumbersome. We have overcome this by considering two different cases where we approximate $T(\mathbf{k}_{g_i}, -\mathbf{k}_{g_i}, \mathbf{k}_{g_j}, -\mathbf{k}_{g_j})$ using the bin averaged trispectrum $\bar{T}(k_i, k_j)$ for which estimates are available from simulations. Results are mainly presented for Case-I which assumes that the different k modes within the same k bin are completely correlated. We also consider Case-II which assumes the different k modes within the same k bin to be totally uncorrelated. These represent two extreme cases, and the reality is expected to be somewhere in between. We find that the error predictions for Case-II are typically intermediate between the Gaussian predictions and Case-I. In most situations we may adopt a simple picture where the predictions for Case-I represent the upper limit for the error covariance matrix, and the actual errors may be expected to have values between these and the Gaussian predictions. It may however be noted that we do have a few situations where the predictions for Case-II exceed those for Case-I as seen in the lower left panel of Figure 6.

We find that the predicted errors typically increase at large k

(Figure 1) where it is system noise dominated. In this situation the r.m.s. error scales as t_{obs}^{-1} , and the k range below which a 5σ detection of the EoR 21-cm PS is possible (k_m) increases as t_{obs} is increased (Figure 2). The values of k_m also increase as reionization proceeds as T_{sys} increases with redshift. At all z a 5σ detection is possible for 128 hrs of observation. However k_m is largest ($\sim 0.9 \text{ Mpc}^{-1}$) at $z = 8$, and the accessible k range is smaller at higher z with $k_m \sim 0.09 \text{ Mpc}^{-1}$ at $z = 13$. The value of k_m increases significantly for $t_{\text{obs}} = 1,024$ hrs and we have $k_m > 1 \text{ Mpc}^{-1}$ for all $z \leq 10$. We have $k_m > 1 \text{ Mpc}^{-1}$ at all redshifts for $t_{\text{obs}} = 10,000$ hrs. We note that at redshifts $z = 7$ and 9 a 5σ detection is not possible at the smallest k bin ($k = 0.04 \text{ Mpc}^{-1}$) which is predicted to be cosmic variance limited (Figures 1 and 4).

The error predictions here are in excess of the Gaussian predictions which ignore the contribution from the trispectrum. At all z the fractional deviation Δ is found to exhibit a "U" shaped k dependence (Figure 3) in the CV limit where the system noise can be ignored. The deviations are minimum at $k_{\text{min}} \sim 0.1 - 0.3 \text{ Mpc}^{-1}$ where the ratio $N_{k_i} \bar{T}(k_i, k_i) / \bar{P}^2(k_i)$ also is minimum, and Δ rises steeply on both sides with particularly large values ($\sim 100\%$) at $k > k_{\text{min}}$. For finite observation times where the system noise is important, we have significant deviations ($\Delta \sim 40 - 100\%$) at $k < k_{\text{min}}$ for $t_{\text{obs}} = 1,024$. However, for $k > k_{\text{min}}$ the errors are system noise dominated (except at $z \leq 8$) and the deviations are small. At $z = 7$ we have particularly large deviations ($\Delta \sim 100\%$ and larger) at $k > k_{\text{min}}$ for $t_{\text{obs}} \geq 1,024$ hrs.

The SNR (Figures 5 and 6) is expected to increase $\propto t_{\text{obs}}$ for small observation time where the system noise dominates the errors, we also expect the Gaussian predictions to match those for Case-I and Case-II in this regime. This is clearly seen for most redshifts at $k = 0.57 \text{ Mpc}^{-1}$ (Figure 5) and 1.63 Mpc^{-1} (Figure 6) which are respectively representative of intermediate and small length-scales. However at $z = 7$ we see that the SNR saturates at the CV limit beyond $t_{\text{obs}} \sim 10^3$ hrs. At $k = 0.04 \text{ Mpc}^{-1}$ (Figure 4), which is representative of large length-scales, the SNR saturates within ~ 100 hrs at all redshifts. The Gaussian predictions, Case-I and Case-II also differ significantly, and the predictions for Case-II are typically between the Gaussian and Case-I predictions.

The inherent non-Gaussianity of the EoR 21-cm signal introduces correlations between the errors in different k bins. Although \mathbf{C}_{ij} ($i \neq j$) is independent of t_{obs} , the dimensionless correlation coefficients $r_{ij} = \mathbf{C}_{ij} / \sqrt{\mathbf{C}_{ii} \mathbf{C}_{jj}}$ are t_{obs} dependent. We expect the correlations r_{ij} to become important for large t_{obs} , and we

have presented results for 1,024 hrs (Figure 7). We find significant correlations and anti-correlations $|r_{ij}| \sim 0.1 - 0.4$ among the four smallest k bins over the entire z range. Further, we find strong correlations $r_{ij} \sim 0.7 - 0.8$ among some of the k bins in the range $k \sim 0.1 - 1 \text{ Mpc}^{-1}$ at $z = 7$ and 9.

The results summarized till now has not considered the foregrounds. The foreground contamination is expected to be restricted within a wedge, and only the k modes outside this foreground wedge can be used for 21-cm PS detection. In addition to the Optimistic scenario where there are no foregrounds, we have also considered the Moderate and Pessimistic scenarios where the $(k_{\perp}, k_{\parallel})$ extent of the foreground wedge respectively correspond to $\theta_L = 3 \times \text{FWHM}/2$ and $\theta_L = 90^\circ$ in equation (16). We find that for both the foreground scenarios a few k bins are excluded and the SNR is reduced compared to the Optimistic scenario (Figure 8). The impact of non-Gaussianity on the error predictions is also reduced (Figure 9). The results for the Moderate scenario are comparable to those for the Optimistic scenarios which has no foregrounds, however the predictions are considerably degraded for the Pessimistic scenario. Finally we note that the deviations from the Gaussian predictions, including correlations between the different k bins, continue to be important ($> 50\%$) for all the scenarios at $z = 7$.

In conclusion we note that non-Gaussian effects make a significant contribution to the error predictions, particularly at low redshifts and large length-scales. In addition to increasing the error predictions with respect to the Gaussian predictions, it also introduces significant correlations and anti-correlations between different k bins.

ACKNOWLEDGMENTS

The authors would like to thank Dr. Raghunath Ghara and Srijita Pal for the help related to the specifications of SKA-Low and baseline distributions. AKS would like to thank Dr. Anjan K. Sarkar, Debanjan Sarkar and Suman Chatterjee for the fruitful discussions. RM would like to acknowledge funding from the Science and Technology Facilities Council [grant numbers ST/F002858/1 and ST/I000976/1] and the Southeast Physics Network (SEPNet).

REFERENCES

- Ali S. S., Bharadwaj S., Chengalur J. N., 2008, *Monthly Notices of the Royal Astronomical Society*, 385, 2166
- Ali Z. S., et al., 2015, *The Astrophysical Journal*, 809, 61
- Bag S., Mondal R., Sarkar P., Bharadwaj S., Sahni V., 2018, *MNRAS*, p. sty714
- Beardsley A. P., et al., 2013, *MNRAS: Letters*, 429, L5
- Beardsley A. P., et al., 2016, *The Astrophysical Journal*, 833, 102
- Becker R. H., et al., 2001, *The Astronomical Journal*, 122, 2850
- Becker G. D., Bolton J. S., Madau P., Pettini M., Ryan-Weber E. V., Venemans B. P., 2015, *MNRAS*, 447, 3402
- Bernardi, G. et al., 2009, *A&A*, 500, 965
- Bernardi, G. et al., 2010, *A&A*, 522, A67
- Bharadwaj S., Ali S. S., 2004, *MNRAS*, 352, 142
- Bharadwaj S., Ali S. S., 2005, *MNRAS*, 356, 1519
- Bharadwaj S., Pandey S. K., 2005, *MNRAS*, 358, 968
- Bharadwaj S., Sethi S. K., 2001, *Journal of Astrophysics and Astronomy*, 22, 293
- Bharadwaj S., Srikant P. S., 2004, *Journal of Astrophysics and Astronomy*, 25, 67
- Bonaldi A., Brown M. L., 2015, *Monthly Notices of the Royal Astronomical Society*, 447, 1973
- Chapman E., et al., 2015, in *Advancing Astrophysics with the Square Kilometre Array (AASKA14)*, p. 5 ([arXiv:1501.04429](#))
- Chatterjee S., Bharadwaj S., 2018, *MNRAS*, 483, 2269
- Choudhuri S., Bharadwaj S., Ghosh A., Ali S. S., 2014, *MNRAS*, 445, 4351
- Choudhuri S., Bharadwaj S., Roy N., Ghosh A., Ali S. S., 2016a, *Monthly Notices of the Royal Astronomical Society*, 459, 151
- Choudhuri S., Bharadwaj S., Chatterjee S., Ali S. S., Roy N., Ghosh A., 2016b, *MNRAS*, 463, 4093
- Choudhury T. R., Haehnelt M. G., Regan J., 2009, *MNRAS*, 394, 960
- Dai W.-M., Ma Y.-Z., Guo Z.-K., Cai R.-G., 2018, preprint, ([arXiv:1805.02236](#))
- Datta A., Bowman J. D., Carilli C. L., 2010, *The Astrophysical Journal*, 724, 526
- Datta K. K., Mellema G., Mao Y., Iliev I. T., Shapiro P. R., Ahn K., 2012, *MNRAS*, 424, 1877
- Datta K. K., Jensen H., Majumdar S., Mellema G., Iliev I. T., Mao Y., Shapiro P. R., Ahn K., 2014, *MNRAS*, 442, 1491
- Davis M., Efstathiou G., Frenk C. S., White S. D. M., 1985, *ApJ*, 292, 371
- Ewall-Wice A., Hewitt J., Mesinger A., Dillon J. S., Liu A., Pober J., 2016, *MNRAS*, 458, 2710
- Faisst A. L., Capak P., Carollo C. M., Scarlata C., Scoville N., 2014, *The Astrophysical Journal*, 788, 87
- Fan X., Narayanan V. K., Strauss M. A., White R. L., Becker R. H., Pentericci L., Rix H.-W., 2002, *The Astronomical Journal*, 123, 1247
- Fan X., et al., 2006, *The Astronomical Journal*, 132, 117
- Fixsen D. J., et al., 2011, *The Astrophysical Journal*, 734, 5
- Gallerani S., Choudhury T. R., Ferrara A., 2006, *MNRAS*, 370, 1401
- Ghosh A., Bharadwaj S., Ali S. S., Chengalur J. N., 2011, *MNRAS*, 418, 2584
- Ghosh A., Prasad J., Bharadwaj S., Ali S. S., Chengalur J. N., 2012, *MNRAS*, 426, 3295
- Greig B., Mesinger A., 2015, *MNRAS*, 449, 4246
- Harker G., et al., 2009, *Monthly Notices of the Royal Astronomical Society*, 397, 1138
- Jacobs D. C., et al., 2016, *The Astrophysical Journal*, 825, 114
- Jensen H., et al., 2013, *MNRAS*, 435, 460
- Jensen H., Hayes M., Iliev I. T., Laursen P., Mellema G., Zackrisson E., 2014, *MNRAS*, 444, 2114
- Kapahtia A., Chingangbam P., Appleby S., Park C., 2018, *Journal of Cosmology and Astroparticle Physics*, 2018, 011
- Kerrigan J. R., et al., 2018, *The Astrophysical Journal*, 864, 131
- Konno A., et al., 2014, *The Astrophysical Journal*, 797, 16
- Koopmans L., et al., 2014, *Advancing Astrophysics with the Square Kilometre Array*, p. 001
- Majumdar S., Bharadwaj S., Choudhury T. R., 2013, *MNRAS*, 434, 1978
- Majumdar S., Pritchard J. R., Mondal R., Watkinson C. A., Bharadwaj S., Mellema G., 2018, *MNRAS*, 476, 4007
- McGreer I. D., Mesinger A., Fan X., 2011, *MNRAS*, 415, 3237
- McQuinn M., Zahn O., Zaldarriaga M., Hernquist L., Furlanetto S. R., 2006, *The Astrophysical Journal*, 653, 815
- Mellema G., et al., 2013, *Experimental Astronomy*, 36, 235
- Mitra S., Ferrara A., Choudhury T. R., 2013, *MNRAS: Letters*, 428, L1
- Mitra S., Choudhury T. R., Ferrara A., 2015, *MNRAS: Letters*, 454, L76
- Mondal R., Bharadwaj S., Majumdar S., Bera A., Acharyya A., 2015, *MNRAS: Letters*, 449, L41
- Mondal R., Bharadwaj S., Majumdar S., 2016, *MNRAS*, 456, 1936
- Mondal R., Bharadwaj S., Majumdar S., 2017, *MNRAS*, 464, 2992
- Mondal R., Bharadwaj S., Datta K. K., 2018, *MNRAS*, 474, 1390
- Mondal R., Bharadwaj S., Iliev I. T., Datta K. K., Majumdar S., Shaw A. K., Sarkar A. K., 2019, *MNRAS: Letters*, 483, L109
- Morales M. F., Hewitt J., 2004, *The Astrophysical Journal*, 615, 7
- Morales M. F., Bowman J. D., Hewitt J. N., 2006, *The Astrophysical Journal*, 648, 767
- Morales M. F., Hazelton B., Sullivan I., Beardsley A., 2012, *The Astrophysical Journal*, 752, 137
- Ota K., et al., 2017, *The Astrophysical Journal*, 844, 85
- Quichi M., et al., 2010, *The Astrophysical Journal*, 723, 869
- Paciga G., et al., 2013, *MNRAS*, 433, 639

- Parsons A. R., Pober J. C., Aguirre J. E., Carilli C. L., Jacobs D. C., Moore D. F., 2012, *The Astrophysical Journal*, 756, 165
- Parsons A. R., et al., 2014, *The Astrophysical Journal*, 788, 106
- Patil A. H., et al., 2014, *MNRAS*, 443, 1113
- Planck Collaboration et al., 2014, *A&A*, 571, A16
- Planck Collaboration et al., 2016a, *A&A*, 596, A107
- Planck Collaboration et al., 2016b, *A&A*, 596, A108
- Pober J. C., et al., 2013, *The Astrophysical Journal*, 768, L36
- Pober J. C., et al., 2014, *The Astrophysical Journal*, 782, 66
- Pober J. C., Greig B., Mesinger A., 2016a, *MNRAS: Letters*, 463, L56
- Pober J. C., et al., 2016b, *The Astrophysical Journal*, 819, 8
- Robertson B. E., et al., 2013, *The Astrophysical Journal*, 768, 71
- Robertson B. E., Ellis R. S., Furlanetto S. R., Dunlop J. S., 2015, *The Astrophysical Journal Letters*, 802, L19
- Santos S., Sobral D., Matthee J., 2016, *MNRAS*, 463, 1678
- Sarkar T. G., Bharadwaj S., 2013, *Journal of Cosmology and Astroparticle Physics*, 2013, 023
- Scott D., Rees M. J., 1990, *MNRAS*, 247, 510
- Shimabukuro H., Yoshiura S., Takahashi K., Yokoyama S., Ichiki K., 2017, *MNRAS*, 468, 1542
- Songaila A., Cowie L. L., 2010, *The Astrophysical Journal*, 721, 1448
- Sunyaev R. A., Zeldovich Y. B., 1972, *A&A*, 20, 189
- Yatawatta, S. et al., 2013, *A&A*, 550, A136
- Yoshiura S., Shimabukuro H., Takahashi K., Momose R., Nakanishi H., Imai H., 2015, *MNRAS*, 451, 266
- Zaroubi S., et al., 2012, *MNRAS*, 425, 2964
- Zheng Z.-Y., et al., 2017, *The Astrophysical Journal Letters*, 842, L22

This paper has been typeset from a $\text{\TeX}/\text{\LaTeX}$ file prepared by the author.